Combustion Theory and Modelling
Vol. 12, No. 4, August 2008, 605–620

Analytical predictions of shapes of laminar diffusion flames in microgravity and earth gravity

S.S. Krishnan[a,*], J.M. Abshire[b], P.B. Sunderland[c], Z.-G. Yuan[d] and J.P. Gore[e]

[a]Department of Mechanical Engineering, Purdue School of Engineering and Technology, Indiana University-Purdue University Indianapolis, Indianapolis, IN 46202; [b]Lockheed Martin Corp., Manassas, VA 20110; [c]Department of Fire Protection Engineering, University of Maryland, College Park, MD 20742; [d]NASA Glenn Research Center, Cleveland, OH 44135; [e]School of Mechanical Engineering, Purdue University, West Lafayette, IN 47907, USA

Flame shape is an important observed characteristic of flames that can be used to scale flame properties such as heat release rates and radiation. Flame shape is affected by fuel type, oxygen levels in the oxidiser, inverse burning and gravity. The objective of this study is to understand the effect of high oxygen concentrations, inverse burning, and gravity on the predictions of flame shapes. Flame shapes are obtained from recent analytical models and compared with experimental data for a number of inverse and normal ethane flame configurations with varying oxygen concentrations in the oxidiser and under earth gravity and microgravity conditions. The Roper flame shape model was extended to predict the complete flame shapes of laminar gas jet normal and inverse diffusion flames on round burners. The Spalding model was extended to inverse diffusion flames. The results show that the extended Roper model results in reasonable predictions for all microgravity and earth gravity flames except for enhanced oxygen normal diffusion flames under earth gravity conditions. The results also show trends towards cooler flames in microgravity that are in line with past experimental observations. Some key characteristics of the predicted flame shapes and parameters needed to describe the flame shape using the extended Roper model are discussed.

Keywords: flame shapes; Roper model; microgravity; inverse diffusion flames; oxygen enhanced

Nomenclature

C coupling function $= (f\text{-}f_a)/(f_0\text{-}f_a)$
d burner diameter
D mass diffusivity
f $\bar{\nu}X_F - X_{O2}$
Fr Froude number $= u_0^2/gd$
g acceleration owing to gravity on earth $= 9.81\ m/s^2$
I_0 Bessel function

*Corresponding author. Email: sskris@iupui.edu

ISSN: 1364-7830 print / 1741-3559 online

DOI: 10.1080/13647830801966146
http://www.tandf.co.uk/journals

$\dot{m}$	mass flow rate
MW	Molecular weight
Q	heat release rate
r	radial coordinate
r_D	characteristic scale of diffusion
Re	Reynolds number $= u_0 d/\nu$
t	residence time
T	temperature
T_{ch}	representative temperature for a flame or, for a flame in which the temperatures vary, the maximum such temperature
u	axial velocity component
v	radial velocity component
X	mole fraction
z	axial coordinate
Z_{st}	stoichiometric mixture fraction, i.e. the stoichiometric mass fraction of material that originated in the fuel supply
Z'_{st}	stoichiometric mass fraction of material that originated in the burner stream, i.e. Z_{st} for NDFs and 1-Z_{st} for IDFs.

Greek characters

α	empirical value selected to match measured flame lengths with Roper predictions $= (T_{ch} - T_0)/(T_{ad} - T_0)$
η	dimensionless r coordinate
ν	viscosity
$\bar{\nu}$	number of moles of O_2 that react stoichiometrically with one mole of fuel
θ	dimensionless z coordinate

Subscripts

a	ambient condition
ad	adiabatic
F	fuel supply
max	maximum value in the associated flame
O_2	oxygen
ox	oxidiser supply
st	stoichiometric condition
0	initial burner condition

1. Introduction

Laminar diffusion flames in microgravity provide a simpler model configuration to study the fundamentals of combustion without the effects of buoyancy. The study of steady non-flickering laminar diffusion flames is an important first step towards understanding more complex turbulent flames. Therefore, a number of experimental and theoretical studies have looked at microgravity laminar diffusion flames and their shapes and soot emissions [1–5]. Laminar inverse diffusion flames (IDFs) have been studied by a number of researchers because of their fundamental importance to understanding soot processes [6–9]. The IDF configuration is also of importance to some

possible fire scenarios on board spacecraft or extra vehicular activity (EVA) environments where a high velocity jet of nearly pure oxygen (O_2) may encounter fuel [10]. Turbulent IDFs using enhanced oxygen have been reported to be most effective in increasing thermal radiation [11]. IDF configurations in which O_2 concentrations in the oxidiser are high have been encountered in fire scenarios aboard spacecraft as well as in terrestrial environments where oxygen is used for life support.

A number of computational studies have been successful in predicting flame structure and other flame properties of jet diffusion flames (see [12, 13] and the references therein). Analytical models have also been valuable tools for understanding and characterising the effects of parameters such as pressure and gravity on flame shapes and lengths [1–5, 14] as well as for the design of new combustion systems [15–19]. Further, flame length is a useful parameter in determining scaling relationships for flame properties such as heat release rates and radiation [20, 21].

In view of the interest in microgravity combustion, IDFs, and the effects of oxygen-enhanced combustion, this study focuses on analytical models for predicting the shapes of laminar normal and inverse diffusion flames at various O_2 contents and gravity levels. The earliest flame shape model was the Burke–Schumann model [22], that included axial convection and radial diffusion effects while ignoring axial diffusion and radial convection effects. Two models commonly used more recently in predicting the flame shapes are the Roper model [23, 24] and the Spalding model [25]. The Roper model assumes that temperature and velocity are constant at each axial location but allows these quantities to vary with z. Thus one may specify axial velocity and/or temperature variations to account for buoyancy and heat loss. Further, the Roper model is not based on a similarity solution and is hence applicable over the entire domain. However, the Roper model does not include the effect of axial diffusion. The Spalding model assumes the Schlichting [26] jet velocity profile and relates a conserved scalar, the mixture fraction, to the velocity profile assuming equal rates of diffusion of species and momentum. This model does not include the effects of buoyancy, property variation with temperature or axial diffusion. In the three models discussed above, axial diffusion effects are neglected. Therefore, these models may not be applicable to microscale diffusion flames such as described in references [16–19] where axial diffusion effects may be important. Finally, Chung and Law [27] extended the Burke-Schumann model [22] for flame shape to include axial diffusion effects and presented the results for the slot burner geometry. However, the axial velocity is assumed constant in both these models. Table 1 summarises the four analytical models discussed above along with their limiting assumptions for comparison purposes.

Sunderland *et al*. [28] extended the Roper model (this will be called the extended Roper model here) to predict complete flame shapes (instead of just flame lengths) assuming uniform velocity and temperature throughout the flame. This extension was considered in the recent textbook by Annamalai and Puri [29]. Xu *et al*. [4] studied non-buoyant laminar diffusion flames and used a simplified analysis following Spalding [25] and Lin *et al*. [2] for predicting flame shapes. This model was based on boundary layer approximations along with a virtual origin and a constant that is fixed based on whether stoichiometric or luminosity lengths are predicted. These two parameters were obtained by fitting experimental data. This model, referred to here as the extended Spalding model, resulted in predictions of both luminous and non-luminous flame shapes covering a wide range of coflow and gravity conditions [4, 5]. Sunderland *et al.* [3] studied the flame lengths and widths predicted by various models including the Roper model and concluded that these models were able to predict the lengths of experimental buoyant and non-buoyant laminar normal diffusion flames (NDFs) accurately but noted that very few models could be used to predict flame widths accurately.

Table 1. Analytical models for flame shapes and their limiting assumptions.

Author/ Reference	Axial diffusion	Axial convection	Radial diffusion	Radial convection	Buoyancy effects?	Infinite domain?	Co-flow?
Burke-Schumann [22]*	Neglected	Included‡	Included	Neglected	No	No	Yes
Roper [23]*	Neglected	Included§	Included	Included	Yes§	Yes	No
Spalding [25]*	Neglected	Included	Included	Included	No	Yes	No
Chung and Law [27]†	Included	Included‡	Included	Neglected	No	No	Yes

*Results available for both slot and circular geometry burners.
†Results available for slot geometry burners only.
‡Axial velocity is assumed constant in these models.
§Axial velocity is modeled as a function of z and hence can account for the effects of buoyancy in a limited manner.

The objectives of the present study were to:

1. Understand the effect of assumptions made in the Spalding and the extended Roper model on the shapes of NDFs and IDFs (for a wide range of O_2 concentrations in the oxidiser and under earth gravity and microgravity conditions).
2. Establish the empirical parameters that best match the flame shapes of laminar diffusion flames in earth gravity as well as microgravity for a wide range of O_2 concentrations in the oxidiser using the appropriate models and based on comparisons with experimental data.

Experimental data from microgravity and earth gravity NDFs and IDFs from Sunderland *et al.* [30] were used.

The test conditions for the flames are listed in Table 2.

2. The extended Roper model

The Roper model for analytical prediction of flame lengths assumes the following [23, 24]:

1. Temperature and axial velocity are allowed to vary in the axial direction but are constant at each z location, i.e. these are functions of z but not r.
2. Combustion causes no change in the number of molecules.
3. Axial diffusion is neglected.

Table 2. Test conditions for ethane flames in earth gravity and microgravity [30].

Flame	X_{O2}	T_{ad} (K)	Q (W)	Z_{st}	C_{st}	m_0 (mg/s)	u_0 (mm/s)	Re	Fr (1g)
21	0.21	2258	72	0.059	0.057	1.51	52	39	0.05
21i					0.943	24.4	866	312	13.89
30	0.30	2553	102	0.081	0.079	2.16	74	55	0.10
30i					0.921	24.5	866	310	13.89
50	0.50	2839	171	0.125	0.125	3.60	124	92	0.28
50i					0.875	25.2	866	310	13.89
100	1.00	3082	342	0.211	0.222	7.21	247	185	1.13
100i					0.778	26.9	866	311	13.89

4. The momentum, mass and thermal diffusivities are the same.
5. The effects of radiation are not integral to the model but assumption 1 allows them to be considered approximately.

As a consequence of assumption 1, buoyant acceleration effects can be accounted for by the model.

Roper *et al.* [23, 24] predicted flame lengths based on the above assumptions. The original derivation was in Cartesian coordinates while Sunderland *et al.* [28] converted the equation to cylindrical coordinates as follows

$$v(r, z)\frac{\partial C(r, z)}{\partial r} + u(z)\frac{\partial C}{\partial z} - \frac{D}{r}\frac{\partial}{\partial r}\left(r\frac{\partial C}{\partial r}\right) = 0; \quad 0 \le z < \infty;\ 0 \le r < \infty. \tag{1}$$

The boundary conditions for equation (1) are given by $C(r, 0) = 1$ for $r < d/2$, $C(r, 0) = 0$ for $r > d/2$ and $C \to 0$ in the far field. Equation (1) is solved using the transformation equations (2) and the flame sheet is located where the mixture is stoichiometric.

$$t(z) = \int_0^z \frac{dz}{u}; \quad \eta(r, z) = \frac{r}{r_D(z)}; \quad \frac{d \ln r_D}{dt} = \frac{v}{r}; \quad \theta(t) = D\int_0^t \frac{dt}{r_D^2} \tag{2}$$

Variables t and r_D are the residence time on the flame axis and the characteristic scale of diffusion. Then, equation (1) becomes

$$\frac{\partial C(\eta, \theta)}{\partial \theta} = \frac{1}{\eta}\frac{\partial}{\partial \eta}\left(\eta\frac{\partial C}{\partial \eta}\right) \tag{3}$$

subject to the boundary conditions, $C(\eta, 0) = 1$ for $\eta < 1$ and $C \to 0$ in the far field. The solution to equation (3) is given by [28]

$$C(\eta, \theta) = \frac{e^{-\frac{\eta^2}{4\theta}}}{4\theta}\int_0^1 e^{-\frac{\eta_1}{4\theta}} I_0\left(\frac{\eta(\eta_1)^{\frac{1}{2}}}{2\theta}\right) d\eta_1 \tag{4}$$

where I_0 is the modified Bessel function of the first kind and zero order. Substituting $C = C_{st}$ into equation (4) for a particular fuel and oxidiser combination results in the prediction of the complete flame shape in (η, θ) coordinates. Equation (4) is solved numerically to obtain the contours in (η, θ) coordinates using Romberg integration and Newton–Raphson iterative methods.

The conversion from (η, θ) coordinates to laboratory coordinates is given by the following expressions [28]

$$z = \frac{u_0 d^2}{4D_0}\left(\frac{T_0}{T(z)}\right)^{0.67}\theta; \tag{5}$$

$$r = \frac{d}{2}\left(\frac{u_0}{u(z)}\frac{T(z)}{T_0}\right)^{1/2}\eta. \tag{6}$$

This conversion requires the specification of the axial velocity, u, and the temperature, T as functions of z as discussed later.

Note that the definition of C_{st} follows Roper [23] and is defined on a molar basis as opposed to Z_{st} and Z'_{st}, which are defined on a mass basis and used in other models [1-5]. C_{st} and Z'_{st} are related by equation (7) below:

$$1/Z'_{st} = 1 + (1/C_{st} - 1)MW_{ox}/MW_F \tag{7}$$

2.1. *Flame shapes in (η, θ) coordinates*

Figure 1 shows the contours of the extended Roper model predictions of flame shapes obtained for some common gas fuels in air plotted in (η, θ) coordinates. These contours are functions of C_{st} only. Table 3 gives the values of C_{st} and Z_{st} for these fuels burning in air. The dimensionless flame length decreases with increasing $C_{st.}$ (see Figure 1). If constant velocity and temperature profiles are assumed, the (η, θ) coordinates are directly proportional to the (r, z) coordinates. However, for other assumptions of velocity and temperature profiles the real flame shapes in (r, z) coordinates can be quite different from the profiles of Figure 1.

Figure 2 shows the predicted extended Roper contours for several values of C_{st}. Here η and θ are normalised using their maximum values. For $C_{st} < 0.1$, typical of hydrocarbon fuels burning in air, the normalised Roper contours are nearly identical. This is a useful result since the normalised Roper contour for $C_{st} = 0.05$ in Figure 2 can be used as a good approximation for the Roper shapes of NDFs of pure hydrocarbon fuels burning in air.

The flame shapes shown in Figure 2 can be classified into two groups: (i) $0 < C_{st} < 0.5$, where $\eta_{max} > 1$, and (ii) $0.5 \leq C_{st} \leq 1.0$, where $\eta_{max} = 1$. The range of C_{st} in the first group is

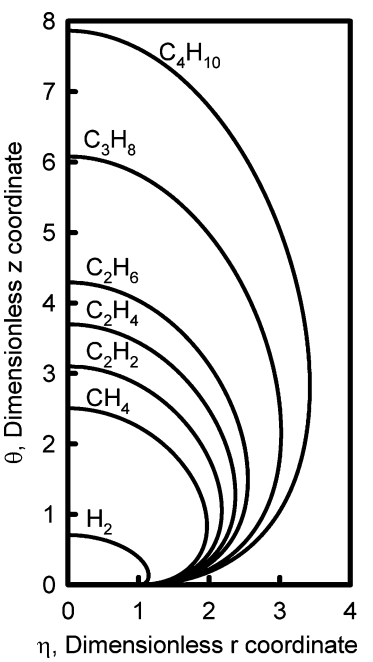

Figure 1. Roper contours of flame sheets in transformed coordinates for normal diffusion flames of common gas fuels in air.

Table 3. Stoichiometric characteristics of NDFs of common gas fuels burning in air.

Fuel	Z_{st}	C_{st}
H_2	0.028	0.296
CH_4	0.055	0.095
C_2H_2	0.070	0.078
C_2H_4	0.064	0.065
C_2H_6	0.059	0.057
C_3H_8	0.060	0.040
C_4H_{10}	0.061	0.031

representative of NDFs of pure hydrocarbon fuels and the shapes in this group exhibit a rounded teardrop shape. In these flames, the widest part of the flame decreases in height as C_{st} increases (see Figure 2).

Note that the flame shapes have an inflection point only for $C_{st} \geq 0.5$. It may be of interest to find when the flame sheet becomes exactly tangential to the burner at the burner exit. i.e. find C_{st} for which the value of $d\eta/d\theta = 0$ at $\eta = 1$. In order to find this point analytically, since $C = C_{st}$, a constant for the flame sheet and $dC/d\theta = \partial C/\partial\theta + (\partial C/\partial\eta)\,(d\eta/d\theta)$, this problem reduces to finding the value of C for which $\partial C/\partial\theta = 0$. It is clear that $\partial C/\partial\theta = 0$ at $\theta = 0$. Therefore, the value of C_{st} at $\eta = 1$, $\theta = 0$ gives the required result from equation (4)

$$C(1,0) = \lim_{\theta\to 0} \frac{e^{-\frac{1}{4\theta}}}{4\theta} \int_0^1 e^{-\frac{\eta_1}{4\theta}} I_0\left(\frac{(\eta_1)^{\frac{1}{2}}}{2\theta}\right) d\eta_1 \tag{8}$$

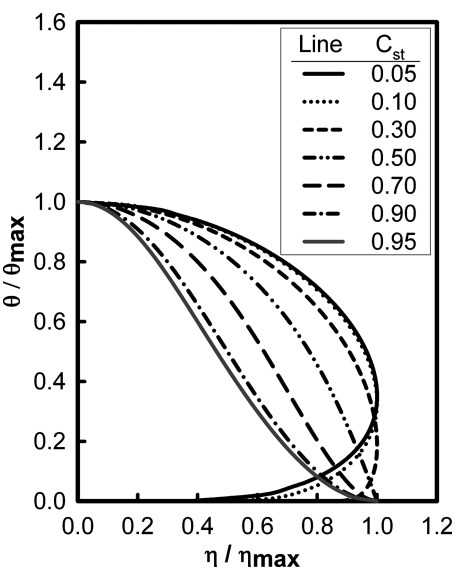

Figure 2. Normalised Roper contours of flame sheets in transformed coordinates for laminar diffusion flames.

The integral in equation (8) is obtained as [31]

$$\int_0^1 e^{-\frac{\eta_1}{4\theta}} I_0\left(\frac{(\eta_1)^{\frac{1}{2}}}{2\theta}\right) d\eta_1 = 2\theta\left(e^{\frac{1}{4\theta}} - e^{-\frac{1}{4\theta}} I_0\left(\frac{1}{2\theta}\right)\right) \tag{9}$$

Equation (8) now reduces to

$$C(1, 0) = \lim_{\theta\to 0} \frac{1}{2}\left(1 - e^{-\frac{1}{2\theta}} I_0\left(\frac{1}{2\theta}\right)\right) = \frac{1}{2} - \lim_{x\to\infty} \frac{I_0(x)}{e^x} = 0.5 \tag{10}$$

Therefore, at $C_{st} = 0.5$ the flame sheet is vertical at $z = 0$. However, owing to numerical accuracy limitations this is not clear in Figure 2.

The range of C_{st} in the second group is representative of IDFs of pure hydrocarbon fuels and the shapes in this group exhibit a needle-like shape which are widest at the base. As C_{st} increases, the flame shape becomes narrower. The shapes become nearly conical for $C_{st} = 0.7$ (see Figure 2).

Figure 3 shows η_{max} and θ_{max} as functions of C_{st}. By setting $\eta = 0$, $\theta = \theta_{max}$ and $C = C_{st}$ in equation (4), the following expression for θ_{max} is obtained

$$\theta_{max} = \frac{-1}{4\ln(1 - C_{st})}. \tag{11}$$

For $C_{st} \geq 0.5$, $\eta_{max} \equiv 1$. However, there is no known closed form expression for η_{max} when $C_{st} < 0.5$. Instead, a polynomial curve fit is obtained from the numerically obtained values of η_{max} for $C_{st} < 0.5$ as follows

$$\eta_{max} \approx 0.7102 + 0.1419(1/C_{st}) - 0.00247(1/C_{st})^2 + 2.13 \times 10^{-5}(1/C_{st})^3 \tag{12}$$

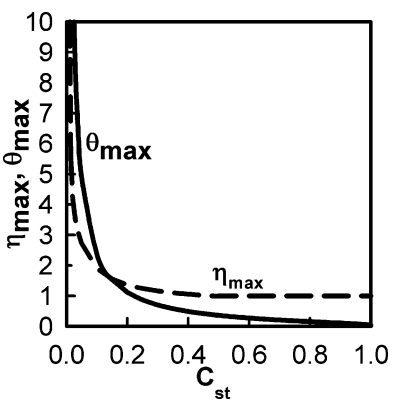

Figure 3. η_{max} and θ_{max} as functions of C_{st}.

2.2. *Flame shapes in laboratory coordinates*

To obtain flame shapes in laboratory coordinates, axial profiles of velocity and temperature need to be specified, as does D_0. Here D_0 is assumed as the mass diffusivity of trace O_2 diffusing into products for NDFs and that of trace fuel diffusing into products for IDFs, both at 298 K. The mass diffusivities were calculated from CHEMKIN [32]. The diffusivity at any axial location, z is given by

$$D = D_0(T(z)/T_0)^{1.67} \tag{13}$$

This study considers two types of axial profiles for temperature, and two for velocity. A discussion of these profiles used to calculate the flame shapes follows in the next section.

2.2.1. *Constant temperature and velocity profiles (Roper$_{u,T}$).*

The simplest assumption is that of a constant temperature, T_{ch} for the regions of the flame where diffusion is dominant, and a constant velocity profile, equations (14) and (15):

$$T(z) = T_{ch} = \alpha T_{ad} + (1 - \alpha)T_0 = \text{constant}; \tag{14}$$

$$u(z) = u_0 = \text{constant}. \tag{15}$$

Roper *et al.* [24] assumed $T_{ch} = 1500$ K for various fuels burning in air under earth gravity. However, the present flames involve consider both microgravity and earth gravity flames. Thus no single T_{ch} for all the flames would be appropriate. Therefore, equation (14) was introduced in this analysis to incorporate a variation in flame temperature for the different cases instead [33]. The value of α was determined using a least-squares fit of the experimental flame lengths for the flames under the four categories (see Table 4).

The flame length is then given by the expression below [23, 24]

$$L_f = -\frac{u_0 d^2}{16 D_0 \ln(1 - C_{st})}\left(\frac{T_0}{T(z)}\right)^{0.67}. \tag{16}$$

2.2.2. *Constant temperature and accelerating velocity profiles (Roper$_T$)*

In the Roper analysis, if alternatively the velocity profile is taken to be accelerating as shown in equation (17) below [23], the flame length is unaffected. The invariance of flame length with axial velocity profiles for circular burners is also reported by Roper [23]. However, the flame width is

Table 4. Summary of assumptions for the Roper calculations.

Model	u(z)	T(z)	Flame Type	Gravity	α	T_{ch} (K)
Roper$_T$	Accelerating	Constant	NDF	1 g	1.00	2223–3082
Roper$_{u,T}$	Constant	Constant	NDF	μ g	0.68	1631–2191
Roper$_*$	Accelerating	Linear	IDF	1 g	0.30	592–716*
Roper$_u$	Constant	Linear	IDF	μ g	0.27	563–674*
Spalding	Deccelerating	Constant	All	All	N/A	—

*Mean temperatures.

narrowed as indicated by equation (6)

$$u(z) = \left[u_0^2 + 2g\left(\frac{T(z)}{T_0} - 1\right)z\right]^{\frac{1}{2}} \tag{17}$$

2.2.3. *Linear temperature and constant velocity profiles (Roper$_u$)*

Since this model allowed variations in the axial temperature, a linear increase in temperature from T_0 at the burner to T_{ch} at the flame tip can be assumed to predict the flame shapes. This profile does not accurately represent the variation of peak temperature in most real gas-jet flames but is nevertheless adopted here for simplicity. Defining T_{ch} for this case based on the maximum temperature (at $z = L_f$) results in the expressions below

$$T(z) = T_0 + \frac{z}{L_f}(T_{ch} - T_0); \tag{18}$$

$$L_f = -\frac{u_0 d^2}{16 D_0 \ln(1 - C_{st})} \frac{(T_{ch}/T_0 - 1)}{(T_{ch}/T_0)^{1.67} \ln(T_{ch}/T_0)} \tag{19}$$

Further note that the temperature, T(z), used here at each axial location, represents a radially averaged temperature in the regions over which diffusion is dominant. In the NDFs considered here, owing to the relatively low convection effects, one may expect the temperatures to remain high in the radial direction within the flame. This will then result in smaller thermal gradients at a particular axial location. Thus, a constant temperature assumption may be appropriate for NDFs. However, due the highly convective nature of the IDFs considered here, there are sharper temperature gradients in the 'diffusion' region. Further, the temperature gradients become smaller with increasing axial location owing to reduced convection effects and increased mixing downstream. Therefore, a linearly increasing temperature profile may be appropriate for IDFs.

For the linear temperature profile, the conversion from (η, θ) coordinates to laboratory coordinates is given by the following implicit equation, which is solved iteratively

$$\theta = \frac{4D_0}{u_0 d^2} \frac{L_f}{(T_{ch}/T_0 - 1)} (T(z)/T_0)^{1.67} \ln(T(z)/T_0)\,. \tag{20}$$

The value of z is obtained from θ iteratively based on equation (20) for θ above and r is obtained from equation (6) after substituting for z. A constant velocity profile, equation (15) was assumed in this analysis.

2.2.4. *Linear temperature and accelerating velocity profiles (Roper$_*$).*

In the above analysis, if the velocity profile is taken to be accelerating as in equation (17) above, the flame length remains unchanged and is obtained from equation (19) above. The flame width is narrowed as indicated by equation (6).

2.3. *The extended Spalding model*

Finally the Spalding model flame shape was obtained following Refs [1–5] as follows

$$r Z'_{st} / d = (3^{1/2})(z/L_f)((z/L_f)^{-1/2} - 1)^{1/2} \tag{21}$$

The flame shapes obtained using the extended Roper model with the four assumptions above labelled as $\text{Roper}_{u,T}$, Roper_{T}, Roper_{u} and Roper_{*} respectively (see Table 4) and the Spalding model for NDFs and IDFs of ethane (C_2H_6) in 21% O_2 are plotted in Figures 4 and 5 respectively.

In all these cases, the parameter α was adjusted to give a flame length of 21 mm, which matches closely the experimental observation for NDFs and is useful for the purposes of comparison. One important observation from Figures 4 and 5 is that although the calculated flame lengths in all these cases match the experimental flame lengths, the prediction of the flame shapes can be unrealistic for some cases. While accelerating velocity profiles are most suitable for earth gravity flames, and constant velocity profiles for microgravity flames, the choice between the constant and linear temperature profiles is based on a comparison of the experimental and predicted flame shapes and discussed further in section 2.2.3 above. Figures 4 and 5 include all the four possible combinations for both NDFs and IDFs for illustration purposes.

The following observations are noted with respect to Figure 4. Constant velocity and constant temperature profiles ($\text{Roper}_{u,T}$) result in a nearly spherical shape that compares well with the experimental flame shapes for microgravity NDFs burning in air. Accelerating velocity and constant temperature profiles (Roper_{T}) result in an elongated flame shape that compares well with the experimental flame shapes for earth gravity NDFs burning in air. Roper_{T} results in a flame shape that spreads outwards near the burner tip. This characteristic is unrealistic. Constant velocity and linear temperature profiles (Roper_{u}) result in an unrealistic flame shape for the microgravity NDF which is narrow at the base but too broad towards the flame tip. Accelerating velocity and linear temperature profiles (Roper_{*}) result in a flame that is broader than the earth gravity NDF. The Spalding model shapes are unrealistically broad for this NDF in either microgravity or earth gravity. Based on these observations and the earlier discussions on temperature gradients in NDFs compared to IDFs, $\text{Roper}_{u,T}$ and Roper_{T} models were chosen to best represent microgravity and earth gravity NDFs respectively.

The following observations are noted with respect to Figure 5. All the predicted IDF flame shapes are narrower than the corresponding NDF shapes as supported by experimental observations. There is very little effect of the velocity profile assumption on the calculated IDF flame

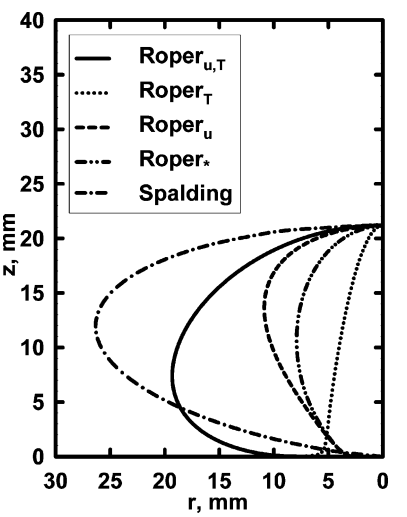

Figure 4. Effect of velocity and temperature profiles on shapes in laboratory coordinates of NDFs of C_2H_6 burning in air.

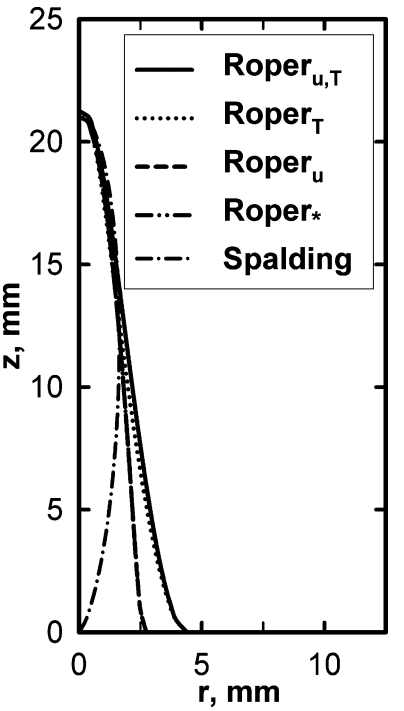

Figure 5. Effect of velocity and temperature profiles on shapes in laboratory coordinates of IDFs of air injecting into C_2H_6.

shapes as expected by the highly convective nature of the IDFs considered here. Linear temperature profiles lead to realistic shapes for IDFs. Constant temperatures ($Roper_{u,T}$ and $Roper_T$) lead to unrealistic shapes for IDFs, i.e. the shapes are too broad at the base. The Spalding model results in reasonable IDF shapes except near the burner exit. Based on these results and the earlier discussions on temperature gradients in NDFs compared to IDFs, $Roper_u$ and $Roper_*$ models were chosen to best represent microgravity and earth gravity IDFs respectively.

The Spalding model predictions shown in Figures 4 and 5 assume decelerating velocities and these result in very wide NDFs. The Spalding model is valid only in the far-field, and the assumption of the Schilchting velocity profile results in the flame shape converging to zero width at the origin. Note that these results do not use a virtual origin [1–5].

3. Comparisons with experiments

The experimental shapes (from Ref. [30]) and the extended Roper shapes for C_2H_6 NDFs with O_2 mole fractions varying between 21 and 100% O_2 are shown in Figure 6. The experimental shapes (from Ref. [30]) and the extended Roper shapes of C_2H_6 IDFs with O_2 mole fractions varying between 21 and 100% O_2 are shown in Figure 7. The horizontal lines indicate the burner plane ($z = 0$). Because the extended Roper shapes do not consider soot, they are best evaluated using blue, not yellow, flame emissions. Stoichiometric conditions are identified by bright blue contours, e.g., that of the 21% O_2 NDF in microgravity. Complete stoichiometric contours are also visible in the 30% O_2 NDF in microgravity, and in all IDFs except the 100% O_2 IDFs. Soot obscures part of the stoichiometric contour in the 21% O_2 NDF in earth gravity, but the lowest 7 mm is visible and this contour is expected to reach the axis near the middle of the yellow

region. Identifying stoichiometric contours is most difficult at 100% O_2 owing to bright soot emissions, and in the case of the 100% O_2 NDF in earth gravity, a broad blue haze. For images where stoichiometric conditions are difficult to identify, referring to flames at lower O_2conditions is generally helpful. Table 4 summarises the assumptions made in calculating the extended Roper flame shapes for these flames. A least squares error fit of the experimental and calculated flame lengths gave $\alpha = 1.00$ and $\alpha = 0.68$ for earth gravity and microgravity NDFs. This resulted in T_{ch} ranging from 2258 – 3082 K for the earth gravity NDFs and ranging from 1631 – 2191 K for the microgravity NDFs respectively as the O_2 mole fraction varied from 21–100% O_2. Cooler T_{ch} are required to match the lengths of the microgravity flames which is consistent with expectations of cooler flames in microgravity owing to increased radiative heat losses. A least squares error fit of the experimental and calculated flame lengths gave $\alpha = 0.30$ and $\alpha = 0.27$ for earth gravity and microgravity IDFs. Note that the values of α reported for the IDFs are based on the peak temperatures at the flame tip. Since the temperature distribution is assumed to be linear in the case of IDFs, an appropriate basis for comparison of the flame temperatures is the mean temperature. The resulting mean temperatures ranged from 592–716 K for the earth gravity IDFs and ranged from 563–674 K for the microgravity IDFs respectively as the O_2 mole fraction varied from 21 - 100% O_2. Low temperatures were required to match the experimental flame shapes of IDFs and this aspect is under further study. Since these IDFs are highly convective, no comparisons were made between the 1g and μg IDFs.

The predicted extended Roper flame shapes of Figures 6 and 7 agree reasonably well with experimental results in all cases except some earth gravity NDFs. The experimental images of the microgravity NDFs show the flames attaching below the burner tip owing to axial diffusion Since axial diffusion is neglected in the Roper model, this characteristic is not seen in the predicted shapes for the microgravity NDFs. However, the nearly spherical shapes (as opposed to a tear-drop shape) calculated by the model are in good agreement with the experimental shapes as can be seen if one shifts the bases of the calculated shapes to match the baselines of the flame images. The predicted flame shapes of the earth gravity NDFs show less agreement with experiments

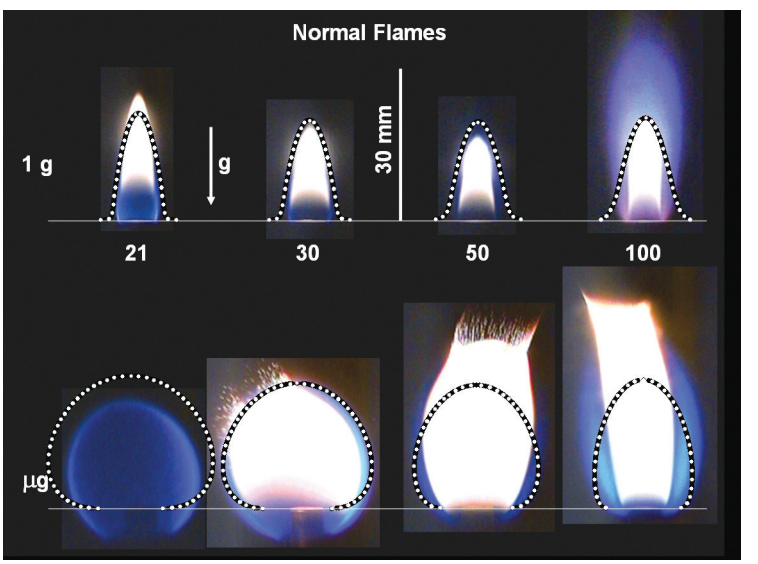

Figure 6. Comparisons of Roper shapes of NDFs (using $Roper_{u,T}$ and $Roper_T$ for μg and 1 g flames respectively) with experimental results (in color) of Ref. [30].

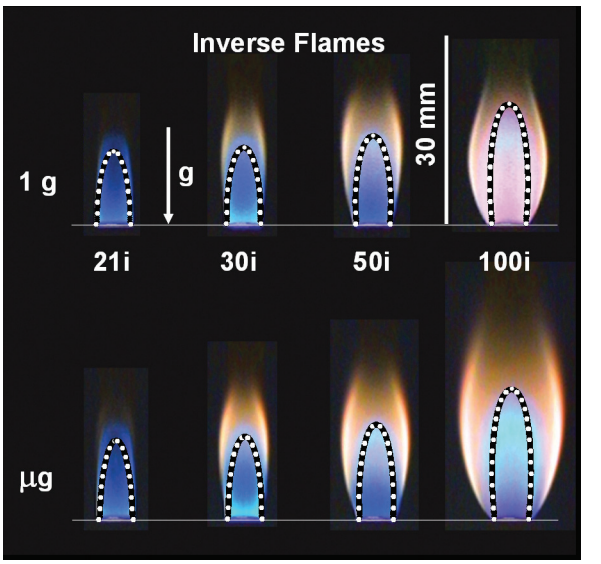

Figure 7. Comparisons of Roper shapes of IDFs (using Roper_u and Roper_* for μg and 1 g flames respectively) with experimental results (in color) of Ref. [30].

especially for higher O_2 concentrations and comparisons are further hampered by the yellow soot region.

Further, it is noted that Froude numbers were in the range of 0.05 to 1.13 for the earth gravity NDFs and were 13.9 for the earth gravity IDFs (Table 2). This indicates the dominance of convection over buoyancy for the IDFs and is further evidenced by the nearly identical earth gravity and microgravity IDF shapes.

4. Conclusions

The Roper flame shape model was extended to predict complete flame shapes of laminar gas jet normal and inverse diffusion flames on round burners. The Spalding model was extended to inverse diffusion flames. The main conclusions were:

1. Results of the extended Roper model compared favourably with the experimental shapes of C_2H_6 IDFs with varying O_2 concentrations and gravity levels. The results of the model predict the nearly spherical shape of the microgravity NDFs but are unable to predict the back-diffusion close to the burner. Obscuration of the flame by soot prevented an exact comparison in the higher oxygen flames. The model predicts the flame lengths of earth-gravity NDFs fairly accurately, but fails close to the burner. The best fit of the flame shapes yielded a value of $\alpha = 1.0$ for NDFs in earth gravity, $\alpha = 0.68$ for NDFs in microgravity and $\alpha = 0.30$ for IDFs in earth gravity and $\alpha = 0.27$ for IDFs in microgravity. This indicates a trend towards cooler microgravity flames compared to earth gravity flames with comparable heat release rates.
2. The extended Roper model is favoured over the Spalding model for the present flames. Although both are capable of predicting flame lengths, the Spalding model overpredicts widths of NDFs, underpredicts widths of IDFs, and cannot account for changes in flame shape arising from changes in gravity level.

3. Reasonable axial velocity and temperature profiles for use in the extended Roper model were established. Constant temperatures are recommended for NDFs which are dominated by buoyancy and linearly increasing temperature profiles are recommended for IDFs which are dominated by convection effects. Accelerating velocity profiles are recommended for earth gravity flames whereas constant velocities are most suitable for microgravity flames.
4. Flame shapes in the transformed coordinate space predicted by the extended Roper model are fundamentally different for C_{st} below and above 0.5. For $C_{st} < 0.5$ the model predicts teardrop-shaped flames without inflection points. For $C_{st} \geq 0.5$, flame contours are predicted to be broadest at their bases and to have inflection points. Flames with $C_{st} = 0.5$ are predicted to have vertical flame contours at their bases. Normalised Roper flame shapes collapse into one shape for NDFs of hydrocarbons burning in air (i.e. $C_{st} < 0.1$).

Acknowledgements

This work was supported by NASA's Office of Biological and Physical Research under the management of Merrill K. King and Dennis P. Stocker. The assistance of David Urban is appreciated.

References

[1] D.L. Urban, Z.-G. Yuan, P.B. Sunderland, G.T. Linteris, J.E. Voss and G.M. Faeth, *Structure and soot properties of nonbuoyant ethylene/air laminar jet diffusion flames*,, AIAA J. 36 (8) (1998), pp. 1346–1360.
[2] K.-C. Lin, G.M. Faeth, P.B. Sunderland, D.L. Urban and Z.-G. Yuan, *Shapes of nonbuoyant round luminous hydrocarbon/air laminar jet diffusion flames*, Combust. Flame. 116 (1999), pp. 415–431.
[3] P.B. Sunderland, B.J. Mendelson, Z.-G. Yuan and D.L. Urban, *Shapes of buoyant and nonbuoyant laminar jet diffusion flames*, Combust. Flame. 116 (1999), pp. 376–386.
[4] F. Xu, Z. Dai and G.M. Faeth, *Flame and soot boundaries of laminar jet diffusion flames*, AIAA J. 40 (12) (2002), pp. 2439–2446.
[5] C. Aalburg, F.J. Diez, G.M. Faeth, P.B. Sunderland, D.L. Urban and Z.-G. Yuan, *Shapes of nonbuoyant round hydrocarbon-fueled laminar-jet diffusion flames in still air,* Combust. Flame. 142 (2005), pp. 1–16.
[6] K.-T. Wu and R.H. Essenhigh, *Mapping and structure of inverse diffusion flames of methane,* Proc. Combust. Inst. 20 (1984), pp. 1925–1932.
[7] G.W. Sidebotham and I. Glassman, *Effect of oxygen addition to a near-sooting ethene inverse diffusion flame*, Combust. Sci. Tech. 81 (1992), pp. 207–219.
[8] L.G. Blevins, R.A. Fletcher, B.A. Benner, Jr., E.B. Steel and G.W. Mulholland, *The existence of young soot in the exhaust of inverse diffusion flames,* Proc. Combust. Inst. 29 (2002), pp. 2325–2333.
[9] C.R. Shaddix, T.C. Williams, L.G. Blevins and R.W. Schefer,*Flame structure of steady and pulsed sooting inverse jet diffusion flames*, Proc. Combust. Inst. 30 (2005), pp. 1501–1508.
[10] B. Burrough, *Dragonfly: NASA and the crisis aboard Mir*, 1st ed., Harper Collins, 1998, pp. 123.
[11] S.S. Hwang and J.P. Gore, *Characteristics of combustion and radiation heat transfer of an oxygen-enhanced flame burner,* Proc. Instn. Mech. Engrs., J. Pwer Energy Part A. 216 (2002), pp. 379–386.
[12] M.D. Smooke, R.J. Hall, M.B. Colket, J. Fielding, M.B. Long, C.S. McEnally and L.D. Pfefferle, *Investigation of the transition from lightly sooting towards heavily sooting co-flow ethylene diffusion flames,* Comb. Theory Model. 8 (3) (2004), pp. 593–606.
[13] X. Qin, C.W. Choi, A. Mukhopadhyay, I.K. Puri, S.K. Aggarwal and V.R. Katta, *Triple flame propagation and stabilization in a laminar axisymmetric jet*, Comb. Theory Model. 8 (2) (2004), pp. 1364–7830.
[14] C.V. Espi, *Analysis of axisymmetric laminar jet diffusion flames for small values of the stoichiometric mixture fraction,* Combust. Sci. Tech. 171 (1) (2001), pp. 1–38.
[15] J.R. Camacho and A.R. Choudhuri, *Shapes of elliptic methane laminar jet diffusion flames*, J. Engrg. Gas Turb. Pwer. 128 (1) (2006), pp. 1–7.
[16] T. S. Cheng, Y.-C. Chao, C.-Y. Wu, Y.-H. Li, Y. Nakamura, K.-Y. Lee, T. Yuan and T.S. Leu, *Experimental and numerical investigation of microscale hydrogen diffusion flames,* Proc. Combust. Inst. 30 (2005), pp. 2489–2497.

[17] T.S. Cheng, C.-P. Chen, C.-S. Chen, Y.-H. Li, C.-Y. Wu and Y.-C. Chao, *Characteristics of microjet methane diffusion flames,* Combust. Theory and Model. 10 (5) (2006), pp. 861–881.
[18] H. Ban, S. Venkatesh and K. Saito, *Convection-diffusion controlled laminar micro flames,* ASME J. Heat Trans. 116 (1994), pp. 954–959.
[19] L.M. Matta, Y. Neumeier, B. Lemon and B.T. Zinn, *Characteristics of Microscale Diffusion Flames,* Proc. Combust. Inst. 29 (2002), pp. 933–939.
[20] G.T. Linteris and I. Rafferty, *Scale model flames for determining the heat release rate from burning polymers*, Proc. 4*th* Int. Sym. Scale Modeling (2003), pp. 231–240.
[21] Y.R. Sivathanu and J.P. Gore, *Total radiative heat loss in jet flames from single point radiative flux measurements,* Combust. Flame. 94 (1993), pp. 265–270.
[22] S.P. Burke and T.E.W. Schumann, *Diffusion flames,* Indust. Eng. Chem. 29 (1928), pp. 998.
[23] F.G. Roper, *The prediction of laminar jet diffusion flame sizes: Part I. Theoretical model,* Combust. Flame 29 (1977), pp. 219–226.
[24] F.G. Roper, C. Smith and A.C. Cunningham, *The prediction of laminar jet diffusion flame sizes: Part II. Experimental verification*, Combust. Flame. 29 (1977), pp. 227–234.
[25] D.B. Spalding, *Combustion and Mass Transfer*, Pergamon Press, 1979, pp. 191.
[26] Schlichting, *Boundary Layer Theory*, 7*th* ed., McGraw Hill, 1979, pp. 171.
[27] S.H. Chung and C.K. Law, *Burke-Schumann flame with streamwise and preferential diffusion,* Combust. Sci. Tech. 37 (1) (1984), pp. 21–46.
[28] P.B. Sunderland, Z.-G. Yuan, and D.L. Urban, *Shapes of buoyant and nonbuoyant methane laminar jet diffusion flames*, Proc. 4*th* Int. Microgravity Combust. Conf. (1997), pp. 129–132.
[29] K. Annamalai and I.K. Puri, *Combustion Science and Engineering,* CRC Press, 2007, pp. 545.
[30] P.B. Sunderland, S.S. Krishnan, J.P. Gore, *Effects of oxygen enhancement and gravity on normal and inverse laminar jet diffusion flames,* Combust. Flame. 136 (2004), pp. 254–256.
[31] I.S. Gradshetyn, I.M. Ryzhik and A. Jeffrey, *Table of integrals, series, and products*, Academic Press, 1994, pp. 717.
[32] R.J. Kee, G. Dixon-Lewis, J. Warnatz, M.E. Coltrin and J.A. Miller, *A Fortran Computer Code Package for the Evaluation of Gas-Phase Multicomponent Transport Properties*, Report No. SAND86-8246, Sandia National Laboratories Report, (1986).
[33] S.C. Li, A.S. Gordon and F.A. Williams,*A simplified method for the computation of Burke-Schumann flames in infinite atmospheres*, Combust. Sci. Technol. 104 (1–3) (1995), pp. 75–91.